



HAL
open science

The path for innovative severe accident neutronics studies in ZPRs - Part I.1 - Analysis of SNEAK-12A experiments for core disruption in LMFBRs

M. Margulis, Patrick Blaise, Fabrizio Gabrielli, Adrien Gruel, Frederic Mellier,
Erez Gilad

► To cite this version:

M. Margulis, Patrick Blaise, Fabrizio Gabrielli, Adrien Gruel, Frederic Mellier, et al.. The path for innovative severe accident neutronics studies in ZPRs - Part I.1 - Analysis of SNEAK-12A experiments for core disruption in LMFBRs. *Progress in Nuclear Energy*, 2017, 94, pp.106-125. 10.1016/j.pnucene.2016.11.001 . cea-02389252

HAL Id: cea-02389252

<https://cea.hal.science/cea-02389252>

Submitted on 2 Dec 2019

HAL is a multi-disciplinary open access archive for the deposit and dissemination of scientific research documents, whether they are published or not. The documents may come from teaching and research institutions in France or abroad, or from public or private research centers.

L'archive ouverte pluridisciplinaire **HAL**, est destinée au dépôt et à la diffusion de documents scientifiques de niveau recherche, publiés ou non, émanant des établissements d'enseignement et de recherche français ou étrangers, des laboratoires publics ou privés.

Interpretation of SNEAK-12A experiment for core disruption in Liquid-Metal Fast Breeder Reactors - The path for innovative severe accident neutronics studies in ZPRs - Part I.1

M. Margulis^{a,b,*}, P. Blaise^a, F. Gabrielli^c, A. Gruel^a, F. Mellier^a, E. Gilad^b

^a*DEN/CAD/DER/SPEX/LPE, CEA Cadarache, CEA Cadarache, Saint-Paul-les-Durance 13108, France*

^b*The Unit of Nuclear Engineering, Ben-Gurion University of the Negev, Beer-Sheva 84105, Israel*

^c*Karlsruhe Institute of Technology (KIT), Hermann-von-Helmholtz-Platz 1, Eggenstein-Leopoldshafen 76344, Germany*

Abstract

The present work details a new benchmark to be produced to the International Community, for dealing with neutronics code validation in the frame of SFRs (Sodium Fast Reactors) severe accidents sequences leading to core degradation and material relocation. The benchmark is based on a complete re-analysis of the SNEAK-12A experimental program, using TRIPOLI-4, MCNP and Serpent-2 Monte Carlo codes as reference tools, and the ERANOS system of codes for deterministic calculations, all based on JEFF-3.1.1 nuclear data libraries. The complete material balance is resumed, and the main degradation sequences are detailed. Preliminary results on available experimental results (k_{eff}) are given, and additional local quantities are calculated, such as axial flux distributions, as well as detector responses in function of the distance to the degraded part. The benchmark offers an excellent opportunity to validate calculation schemes for strongly heterogeneous interfaces, in particular the preparation of homogenized and condensed cross sections for deterministic core calculations, as well as leakage treatment in locally very heterogeneous media. This work is made within the frame of new core design capacities and new ways of conducting experiment in Zero Power Reactors, such as the ZEPHYR project led independently by CEA. The present analysis will be completed by a full nuclear data sensitivity and uncertainty analysis of the reactivity coefficients in a companion paper.

Keywords: SNEAK-12A, Core disruption, Severe accidents, LMFBR

1. Introduction

Severe core accident (SCA) in Liquid Metal-cooled Fast Breeder Reactors (LMFBRs) could occur either due to prompt or super-prompt recriticality or serious loss of heat sink [1]. The progression of a SCA in fast breeder reactors (FBRs) is significantly influenced by the core physics, which is the primary focus of the SNEAK-12A experimental series [2-4], since the core is not assembled in its most reactive configuration. Hence, redistribution processes

*M. Margulis

Email address: marat.margulis@cea.fr, maratm@post.bgu.ac.il (M. Margulis)

of core materials (fuel, sodium, absorbers, or structural materials) can potentially lead to severe power excursion. Therefore, the study of [SCA](#) progression requires an adequate description of the core's neutronic behavior during the different stages of the [SCA](#). Reactivity changes in the core could result from many different reasons, whereas the main contributors are:

- 10 (1) Loss of coolant - this type of accident leads to neutron spectrum hardening and increased neutron leakage.
- (2) Change in material arrangement - could either increase or decrease neutron streaming.
- (3) Redistribution of fuel and structural materials - could lead to streaming effects and changes in the neutron direct and adjoint fluxes.
- (4) Accumulation of relocated fuel in certain regions of the core - could lead to an increase in the core multiplication
15 factor.

These changes can have pronounced influence on the neutronic characteristics of the core, which could severely damage both normal and emergency operation of the reactor. Therefore, in order to predict the core behavior during such disruptions, it is imperative to develop accurate and precise computational and experimental tools and methodologies for studying these phenomena. Furthermore, the validation of computational tools against experimental measurements of critical assemblies that represent different stages of the disrupted core configurations is mandatory for
20 evaluating the code performances and quantify any discrepancies between experiment and theory.

This paper presents a new benchmark problem based on the [SNEAK-12A](#) critical assembly experiments [2, 3]. The SNEAK facility was located at Kernforschungszentrum Karlsruhe (KfK) and was primarily used for experimental examination of reactivity differences between non-disrupted core and a series of disrupted configurations that represented a series of core disruptions of the kind mentioned above. During the program, several neutronic codes, such
25 as SNOW [5], TP2 [6], and the neutronic solver of SIMMER-II [4] were validated against the experimental program results.

It should be noted that the course of events during a hypothetical core disruptive accident in fast reactors, e.g., an unprotected loss of flow (ULOF), is usually described in several phases [7, 8]. Each phase is characterized by a set
30 of physical phenomena. The initial phase of a ULOF deals with the loss of coolant flow (e.g., pump coastdown, main steam line break, etc.) and the subsequent processes that lead to the primary power excursion. This power excursion, if important enough, can initiate local sodium voidage, and hence first local fuel melt. The process initiates material redistribution processes, which start a few seconds after the first melt formation. The neutronics codes used for modeling this accident phase are mainly based on multigroup diffusion approximation, point kinetics model, and first
35 order perturbation calculations. These approximations are valid as long as in-core material redistribution processes have not yet begun. However, as the [SCA](#) progresses into the next phase, where thermal-hydraulic conditions reach their heat transfer limits and gravity acts on molten core materials, the spatial distribution of the neutron flux is dramatically changed, and space-dependent kinetics is required for adequate neutronic modeling of this phase.

The accidents at Chernobyl, Three Mile Island (TMI-2) and, more recently, at Fukushima, allow to better understand a realistic core behavior during a catastrophic event. Degraded core processes are a key factor in progression of a SCA. An in-vessel accident progression is a non-coherent step-wise process, which results in a melting and liquidation of core materials at different temperatures. In fast reactors, one of the major concerns is a recriticality event due to a core disruptive accident (CDA), in which the reactivity is increased due to fuel redistribution in the core [1, 9], thus causing a power transient. The concern in such an event is that the mechanical energy generated during such a transient would compromise the integrity of the reactor vessel and containment building. The conventional way to ensure the integrity of the fast reactor is to impose stricter limits on the primary design of the reactor, which are derived from conventional assumptions (e.g. designs include facilities that could withstand large power excursion). Recent research in the sphere of recriticality possibility in fast reactors focus on mechanisms for preventing the possibility of recriticality event [9–13], without any reference to recriticality possibility due to the failure of the mechanism.

Recriticality accident is of less concern in LWRs (although molten pool can present, in some geometries, recriticality situations), prompt recriticality is a major issue in modern Gen-IV fast reactor safety studies. As an indicator, all past studies on SCA were performed in fast critical facilities. In particular, fuel melting is an intrinsic danger situation if fast reactors as local void fraction in previous design were characterized by a positive power coefficient, hence leading to excursion. The experimental configurations studied in SNEAK-12A were representative of the second phase of in-core material redistribution of varying sizes.

Several other experiments of core disruption were carried out around the world, e.g., ZEBRA-8G and ZEBRA-12 [14], ZPPR-5 [15], ZPPR-9 [16], and FCA VIII-2 [17]. However, among these programs SNEAK-12A was the most comprehensive, with large number of experiments aimed at measuring reactivity changes caused by one of the following: cavities, streaming channels, redistribution of structural material, dispersal and re-compaction of fuel, or formation of molten pools at the bottom of the core.

Therefore, there exists an essential need to re-introduce this benchmark problem to the nuclear community, accompanied by advanced state-of-the-art computer codes calculations and additional critical experiments able to bridge the knowledge gap related to core physics phenomenon. As GEN-IV reactors are mainly foreseen to operate in fast spectrum, this benchmark problem could provide additional information regarding core behavior during progression of a SCA in such reactors from a pure neutronics point of view. This revisit of the SNEAK benchmarks is a first step for a future program, aiming to study neutronic behavior of fast reactor core under SCA that would be implemented in the ZERo power PHYSics Reactor (ZEPHYR) [18].

2. SNEAK-12A- Benchmark Specification

The information regarding SNEAK-12A core outline is mainly stored in the SNEDAX data base [19]. The SNEDAX database contains information on built assemblies and experiments performed in SNEAK (FZK Karlsruhe), MASURCA (CEA Cadarache), ZEBRA (IAEA Winfirth), and RRR (Rossendorf Ringzinnen Reaktor) fast critical fa-

cilities. This section provides a short overview of the [SNEAK-12A](#) core geometry outline, loaded with uranium fuel plates, as described in section 2.1. This was mainly dictated by the availability at the time when the experiments were carried out. The basic fuel cell geometry in the [SNEAK-12A](#) was designed according to the following requirements

75 —

- (1) Fuel cells should be easily loaded into or unloaded from the core.
- (2) Fuel and sodium densities should be easily determined and updated anywhere in the core (including sodium void formation) for the purpose of material redistribution experiments.
- (3) The core neutronic characteristics should be similar to those of a fast spectrum power reactor.

80 In the case of the [SNEAK-12A](#) core the material volume fractions of the fuel, steel and sodium corresponded approximately to those of the SNR-300 reactor [20].

2.1. Core Description

The [SNEAK-12A](#) core consists of horizontal fuel plates assemblies, and is cooled by air, which flows through the gaps between the fuel assemblies. The total core width including unused areas (filled with air) is 326.4×326.4 cm² and total height of about 240 cm. The active region is 130.56×130.56 cm² in area and about 80 cm in height surrounded by 30 cm of upper and lower reflectors, which makes a total of 140 cm. The radial blanket fuel assemblies are slightly longer than the fissile fuel assemblies, leading to a total height of about 150 cm. The core consists of three main radial zones: the radial blanket, the fissile active zone and the test zone that changes from a grid of 4×4 to 6×6 , as shown in Fig. 1. The core reactivity was controlled by 14 shim rods (marked by blue squares in Figure 1) located in the core center zone and 6 shim rods located at the core-blanket boundary.

90

The fuel assembly is a 5.44×5.44 cm rectangular filled with horizontal plates of fuel and sodium, with air flowing between them as coolant. A representative fuel assembly is schematically shown in Figure 2. Most of the fuel assemblies in the core are composed of 35% and 20% enriched uranium metal slabs. The blanket and the axial reflectors consist of depleted uranium dioxide. The full specifications of the [SNEAK-12A](#) are given in Appendix A.

2.2. Experimental configurations

95

The [SNEAK-12A](#) program included a large number of experiments. However, this benchmark covers only a limited number of experiments, which had the most detailed documentation in the SNEDAX data base. Furthermore, the experiments considered in this benchmark were also chosen according to their potential to create a sequence of configurations which would best represent the events initiated by the [SCA](#) phases described above.

100

The first set of experiments represents a sequence of fuel melt down events ([SCA](#) progression), which is initiated by a complete channel voiding. The second stage is a small fuel compaction around the core mid-plane, followed by a large fuel compaction. The last stage is the accumulation of the entire fuel assembly fissile and fertile material content at one end of the core. The different stages are schematically illustrated in Fig. 3. In this work, this sequence

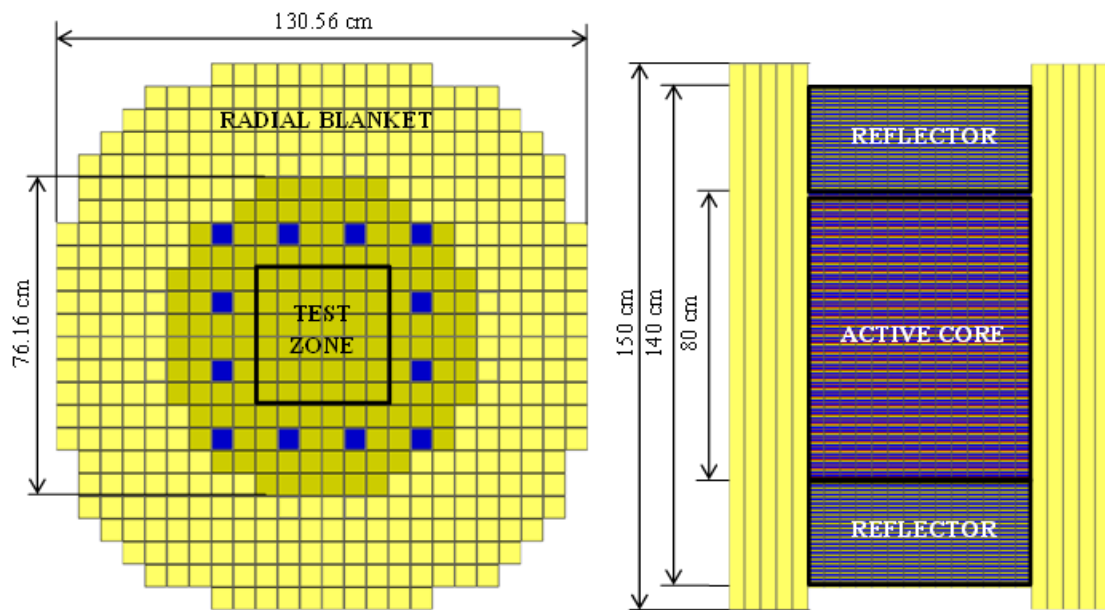


Figure 1: SNEAK-12A core layout and dimensions. The blue squares indicate on the shim rod positions (left - XY cross section, right XZ cross section).

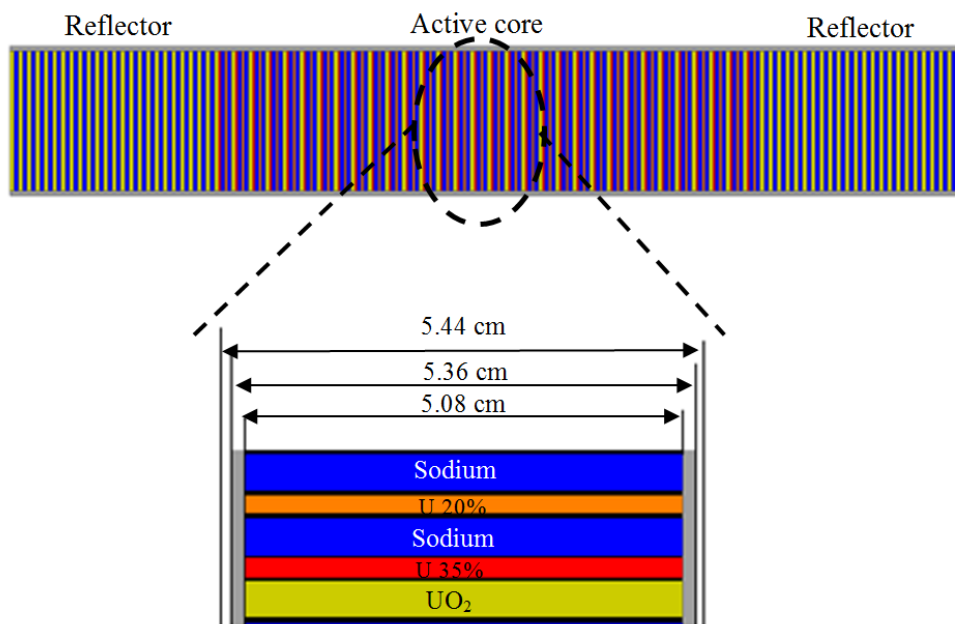


Figure 2: XZ cross section of a typical fuel assembly geometry and ^{EREZ} material composition.

was considered on both small scale (4 affected fuel assemblies) and large scale (16 affected fuel assemblies) at the
105 core center. It should be noted that the total material inventory remains constant during the different stages.

The second set of experiments deals with the accumulation of molten material near one of the axial blanket areas. Fuel was compacted asymmetrically near one of the core boundaries and supported by a low density empty steel box, as seen in Fig. 4, in a varying number of affected fuel elements (from 4 to 36) using the same material configuration in all the affected fuel assemblies, as shown in Fig. 5. In the case of the SNEAK core, the fuel compaction was created
110 at the upper plenum due to the core safety features (shim rods where extracted downwards).

3. Computational tools

Reactivity calculations for the different configurations studied in this work were performed by Monte Carlo (MC) based codes (MCNP5 [21], Tripoli4 [22] and Serpent2 [23]) and by the ERANOS reference deterministic transport code [24]. The nuclear data library used in this study is based on the JEFF-3.1.1 evaluation. Furthermore, the ERA-
115 NOS calculation is performed on a R-Z geometry using a 33 energy group structure for cross section homogenization. This 33-energy mesh, adequate for fast studies, is derived from the international X-MAS 172-energy structure. The MC calculations exact 3-dimensional geometry as specified by the SNEAK-12A benchmark. The calculations are performed based on 200k neutron histories with 500 active and 50 in-active cycles, such as to guarantee a convergence on the k-eff of less than 10 pcm ($10^{-5}\Delta k/k$) and less than 1% on local flux distributions.

120 4. Results

In this section measured and calculated results are compared. In order to obtain an indication of the accuracy of the different codes, results from all different experimental and theoretical methods are cited.

4.1. Clear criticality experiments

The different experiments considered in this section are all referenced to the most basic unperturbed core loading of
125 SNEAK-12A (the reference core). Therefore, it is essential to correctly calculate the reference core. The experimental versus calculated values are summarized in Table 1, where the values on the diagonal are the effective multiplication factor obtained from each code, as the off-diagonal correspond to the relative discrepancies between the different columns (in pcm). As can be seen, there are very small differences between the MC based codes and the experimental value. However, when examining this core in R-Z geometry with ERANOS, the error significantly increases, with an
130 underestimation of the critical state by about 0.6%, as expected from numerous studies. The impact comes mainly from a cylindrization effect of the - almost- square core, combined with a strong simplification of the shim rod insertion, modeled by an homogenized ring of absorber in the RZ geometry.

Unfortunately, there is almost no available data for comparison except the core effective multiplication factor and the reactivity changes between the different configurations. This is due to lack of miniature measurement equipment

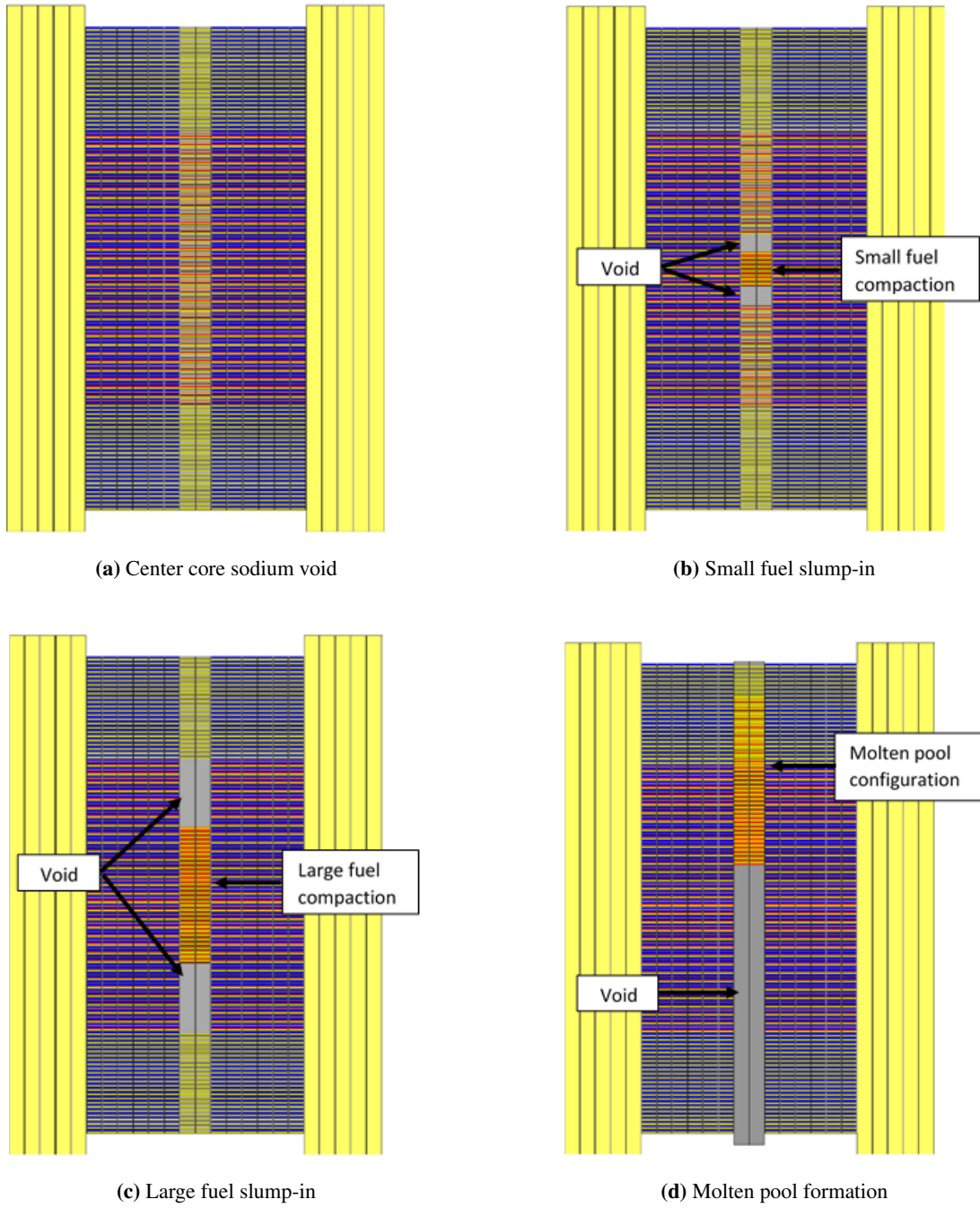


Figure 3: Different stages of SCA progression in the SNEAK-12A core

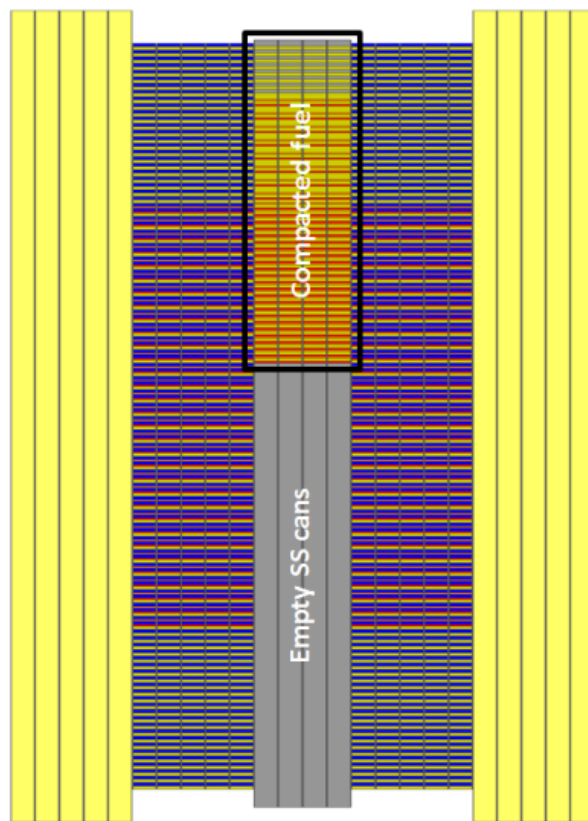


Figure 4: XZ cross section of a molten pool configuration.

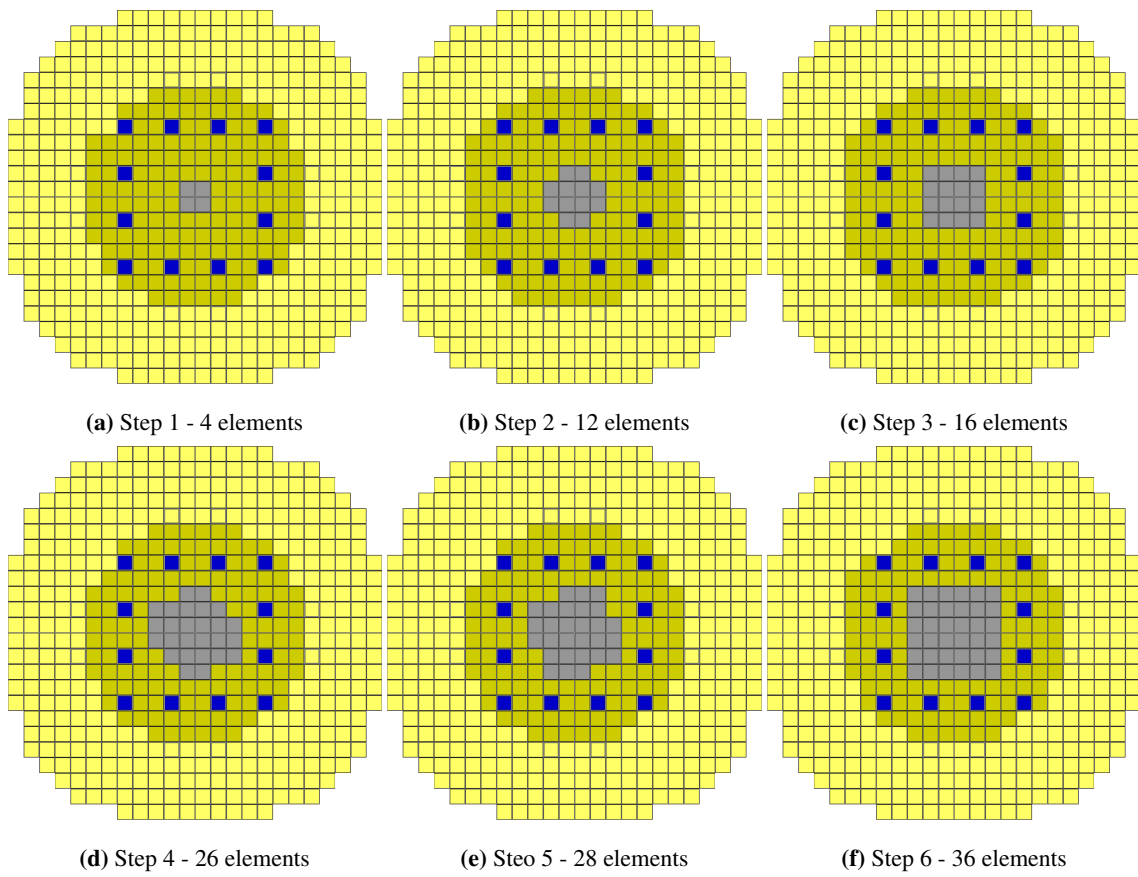
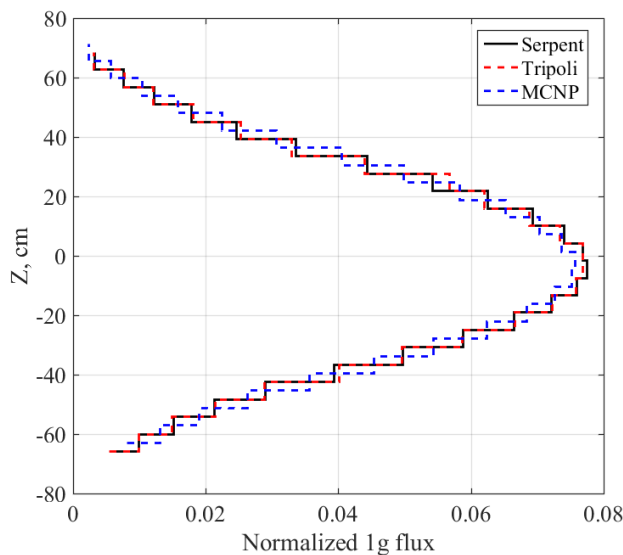


Figure 5: Different stages of molten pool formation

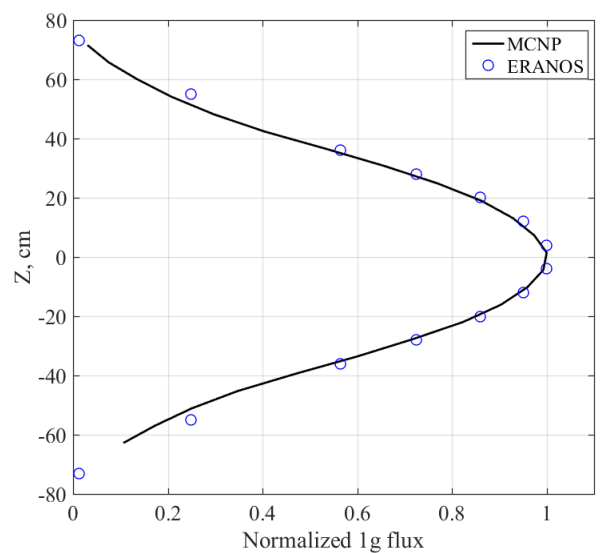
135 that could be fitted in to the tight core arrangement of the the SNEAK. Therefore, a presentation of flux traverses and reaction rates distribution is made for code-to-code comparison only. As shown in Fig. 6, there is an excellent agreement between the integrated axial flux distribution along the core center line that where obtained from the different MC codes and between MCNP and ERANOS for the clear criticality configuration.

Table 1: Comparison of effective multiplication factor obtained from the experiment and the codes for the basic unperturbed configuration of SNEAK-12A

Source	Experimental	Serpent2	Tripoli4	MCNP5	ERANOS(R-Z)
Experimental	1.00075	32.0	-29.9	-91.8	600.1
Serpent2	-	1.00043 ($\pm 7.6E-05$)	-61.9	-123.7	568.1
Tripoli4	-	-	1.00105 ($\pm 8.6E-05$)	-61.8	630.0
MCNP5	-	-	-	1.00167 ($\pm 1.8E-04$)	691.9
ERANOS (R-Z)	-	-	-	-	0.99478



(a) Comparison of MC codes



(b) Comparison of MCNP5 vs. ERANOS

Figure 6: Comparison of integrated axial flux distribution at core center line obtained by different codes

4.2. Molten pool configurations

140 In this series of experiments, in which the fuel was compacted near one axial blanket area (see Fig. 4), the affected area was radially enlarged in several steps. Initially, the experimentally measured reactivity decreases until reaching a minimal value. For larger radii of the affected area, the reactivity rises and at some point becomes positive. This reactivity increase is mainly due to the fact that, for smaller radii, the reactivity changes are mainly governed by the fuel redistribution to regions characterized by lower flux and importance. However, for larger affected area, the
145 increased multiplication in the compacted region predominates.

As shown in Fig. 7 and summarized in Table 2, the MC codes predict the molten pool growth very well with only a small deviation with respect to the experimental data. The only point with large deviation is the final 36 affected element configuration, which was declared as a calculated point in the SNEDAX data base. Unfortunately, there is no explanation on the calculation methodology, or whether it was obtained from code calculation or extrapolated from
150 the experimental results. The R-Z calculation in ERANOS show a similar behavior to the experimental curve for the small molten pool configurations (4, 12 and 16 affected elements). However, for larger molten pool configurations, specially in the region where the reactivity change becomes positive (above 26 affected elements) ERANOS results constantly over estimate the experiment, with a constantly growing discrepancy. It should be noted that some square shaped molten pool configuration (16 and 36 affected elements) introduce additional geometrical uncertainties in
155 the R-Z model. Therefore, the ERANOS prediction was extrapolated from the four configurations that have close to cylindrical shape (4,12 and 28), seen in Fig. 5. The extrapolated ERANOS results then exhibit similar behavior observed in the Helm's original SNEAK-12A analysis with SIMMER-II [20] transport calculation as seen in Fig. 8.

Fig. 9 summarize axial flux distribution obtained from all codes in the 28 affected elements configuration. As depicted from the results, there is a good agreement between all the MC codes, whereas ERANOS clearly under
160 estimates the flux in the voided region ($-80 < Z < 0$) and over estimates it in the molten pool configuration ($0 < Z < 80$). This might be due to the model uncertainties, which arises from the meshing limitations in the deterministic code. Furthermore, from a large amount of dedicated experimental validation from different Na void programs [25], ERANOS is known to slightly underestimate the leakage factor in sodium void patterns. The MCNP results fit close to the other MC codes with some deviation, resulting from a slight shift in the geometrical mesh.

165 4.3. Fuel slump-in experiments

This section summarizes the reactivity effects due to (no axial symmetry in Fig. 3, only radial) redistribution of fuel according to the scheme presented in Fig. 3. The reactivity changes due to the fuel rearrangement are dominant by neutronic effects, which influence the sequence of events in the case of a postulated accident.

170 The small slump-in (Fig. 10 and Table 3) induces a positive reactivity insertion in comparison to the sodium voiding stage. However, the total reactivity remains negative due to the small amount of compacted fuel. On the other hand, the large center core slump-in (Fig. 11 and Table 4) induces a relatively large reactivity insertion, mainly due to large fuel compaction, which reduces the leakage and creates an area of high neutron importance in the core center.

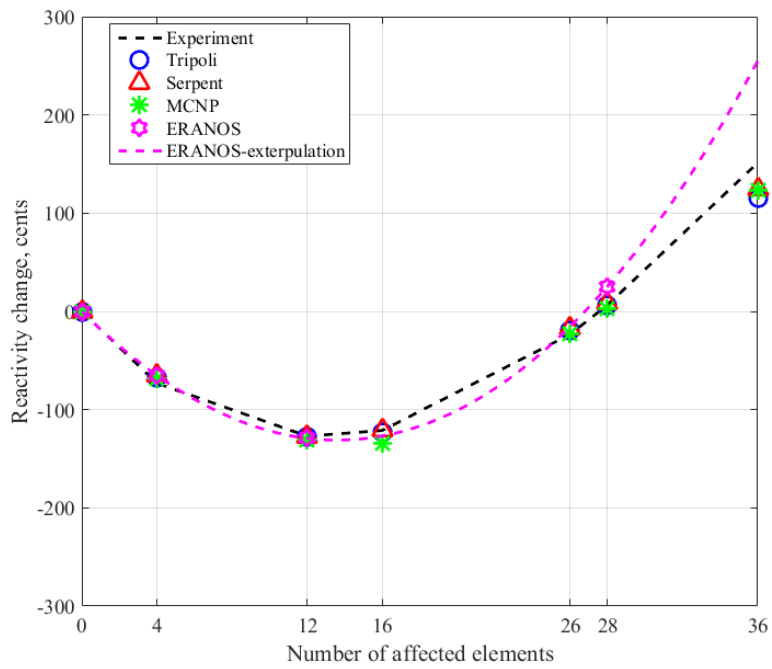


Figure 7: Reactivity versus number of affected elements in the core center

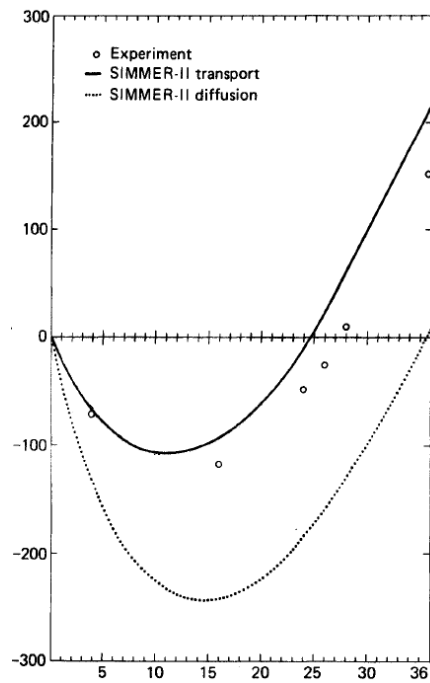


Figure 8: Reactivity versus number of affected elements in the core center computed by SIMMER-II [20]

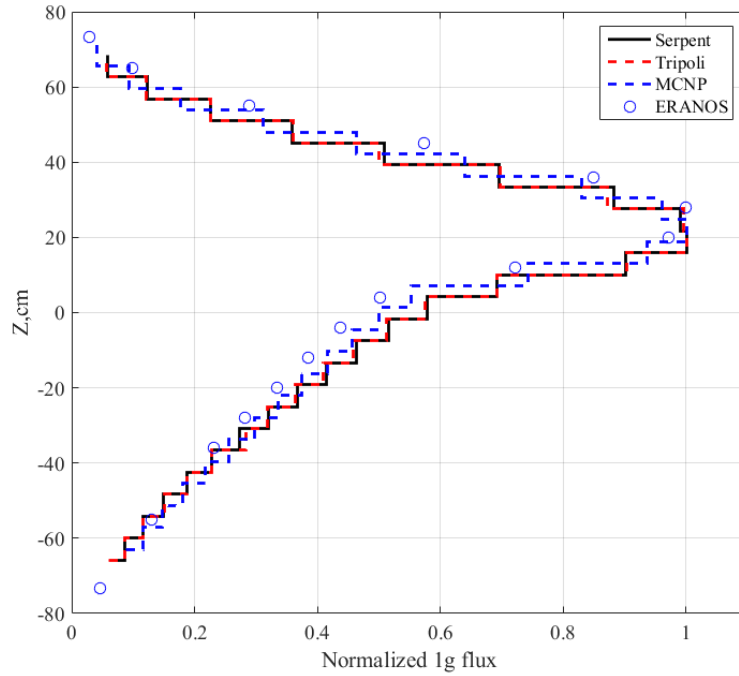


Figure 9: Center line axial flux distribution for 28 affected elements. A comparison between different codes

Table 2: Comparison of reactivity changes between different molten pool configurations obtained from the experiment and the codes.

Affected elem.	Experimental	Serpent2	Tripoli4	MCNP5	ERANOS(R-Z)
0	0	0	0	0	0
4	-73.1	-67.6	-64.8	-68.46	-65.10
12	-127	-127.6	-127.6	-130.71	-129.23
16	-121.2	-123.4	-120.6	-134.61	-
26	-23.4	-19.3	-17.4	-22.87	-
28	6.6	5.8	8.9	3.2	24.61
36	151.3	115.07	124.3	123.05	-

The last stage in the small core distortion (Fig. 10) is the molten pool formation, where the reactivity insertion is negative due to relatively small fuel removal from the high importance region in the core center. The same trend is observed on large scale SCA (Fig. 11). This behavior is similar to the one demonstrated in the molten pool formation analysis (see section 4.2), where 16 molten pool elements induced the most negative reactivity change, as shown in Fig. 7.

The relatively large difference between the MC codes and the experimental data at the large slump-in stage for the large configuration (Fig. 11) is a result of different number of affected elements. The experiment at this stage was performed with 12 affected elements while the simulation were performed with 16 affected elements. It was not possible to carry out such an experiment due to very high reactivity insertion that was followed by the fuel compaction in 16 fuel elements. However, the magnitude of the calculated results is consistent with the smaller experiment results.

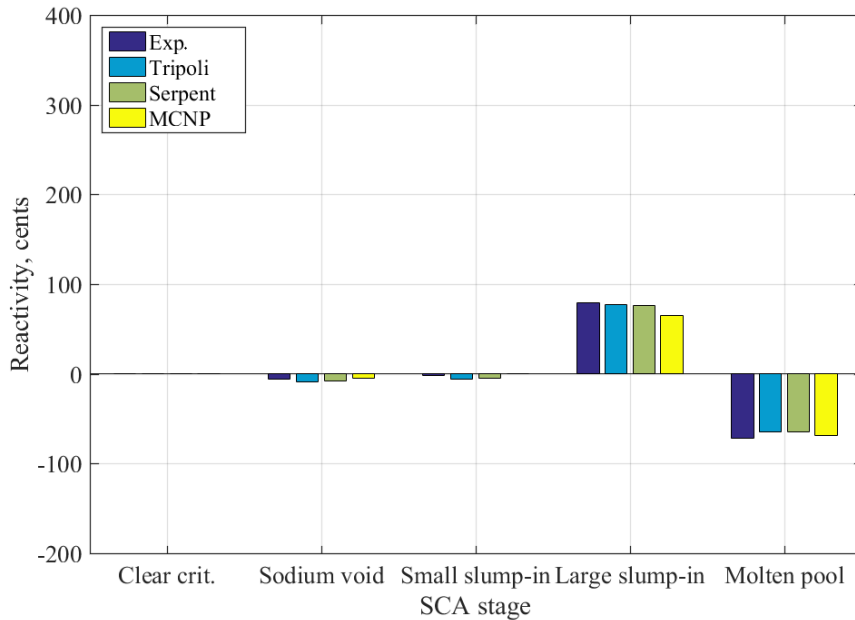


Figure 10: Reactivity changes due to SCA progression for small affected region.

The experimental results support several international studies [26–28] regarding elimination of recriticality possibility in LMFBR reactors, e.g., the Fuel subAssembly with Inner DUct Structure (FAIDUS), studied at the Japan Atomic Energy Agency (JEA) and the Tokyo Institute of Technology (TIT) [9, 10, 13, 28], as well as the CAPRA/CADRA studies on fast burner reactors at CEA Cadarache [29]. All these programs focused on techniques or technological innovative assembly designs for avoiding the high reactivity insertion during the molten pool formation (shown in Fig. 7) via the immediate removal of the melted fuel from the core center to the lower or upper plenums, and then to the core catcher.

Table 3: Comparison of reactivity changes between different small scale SCA progression configurations obtained from the experiment and the codes.

Configuration	Clear	Sodium void	Small slump-in	Large slump-in	Molten pool
Exp.	0	-5.9	-1.4	79.1	-72.2
Serpent	0	-8.5	-5.8	77.1	-65
Tripoli	0	-8.1	-4.6	75.9	-64.5
MCNP	0	-4.7	0.02	65	-68.46

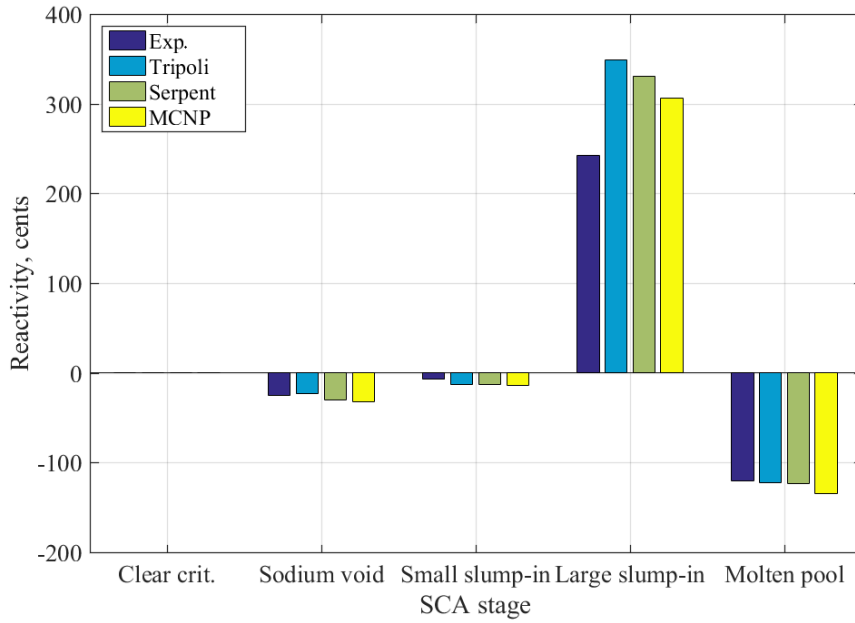


Figure 11: Reactivity changes due to SCA progression for large affected region.

Table 4: Comparison of reactivity changes between different large scale SCA progression configurations obtained from the experiment and the codes.

Configuration	Clear	Sodium void	Small slump-in	Large slump-in	Molten pool
Exp.	0	-25.6	-7.4	242.3	-120
Serpent	0	-23.5	-13.2	349.1	-122.5
Tripoli	0	-29.8	-12.9	331	-123
MCNP	0	-31.9	-14.1	306.1	-134.61

4.4. Monitoring of SCA progression

The prompt detection of early stages of SCA is of up most importance in terms of reactor safety. The sequence of operations to mitigate SCA is dictated by the stage of the accident progression. Therefore, it is essential to determine the SCA initiation point. Unfortunately, during the operation of the SNEAK-12A program, a dedicated detection methodology was not investigated thoroughly due to both technological drawbacks and tight lattice configurations that did not allow the insertion of adequate miniature detector system inside the core. Simulation of ex-core detectors (outside the large blanket region) indicated that it is impossible to derive any meaningful conclusions due to very small neutron leakage rate resulting in poor detector's count rate. In this section, we study a possible solution for early detection of SCA by using in-core detectors, e.g., miniature fission chambers.

In order to be able to predict the behavior of the molten pool configuration, a series of miniature fission chambers were placed in different places on the blanket-core boundary, as shown in Fig. 12. Most of them were made at the shim rods location, which are smaller than the normal core fuel assemblies. Furthermore, location 1 in Figs. 13 and 14 contained two miniature fission chambers, one located at the top end of the active core zone and the second at core mid-plane. For the simulation, two types of miniature fission chambers were considered, a ^{235}U and a ^{242}Pu . The use of ^{242}Pu as fission chamber deposit is known as being the best choice for monitoring fast neutrons in a high neutron flux [30].

The detectors in Fig. 12 correspond to the presented results in Figs. 13 and 14 in the following manner -

- Location 1 - This location corresponds to two detectors presented in Figs. 13 and 14, the "Center in" and the "Center in top" detectors. Those detectors located one above the other on the boundary between the fissile inner core and the fertile blanket.
- Location 2 - This location corresponds to the "Center mid." detector name in Figs. 13 and 14, located at the gap between the normal core fuel assembly and a shim rod.
- Location 3 - This location corresponds to the "Diagonal in" detector name in Figs. 13 and 14, this detector is located at the diagonal shim rod position.

The fission reaction rates in the different detectors are summarized in Fig. 13 and 14. Two distinct trends of the fission chambers behavior are pointed out. The fission rates in all detectors located at mid XY plane are monotonically decreasing, whereas the top end plane detector exhibits monotonic rise in fission reaction rate. Furthermore, the gradient of the fission reaction rate curve exhibited by the top end plane detector is steeper than that of the mid plane fission chambers. This behavior could be used as indication of the molten pool (or fuel melting) growth.

5. Conclusions

The SNEAK-12A program was aimed at validating the neutronics calculation methods for severe accident degraded configurations representative of FBRs. The accident analyses were carried out by measurements and calcula-

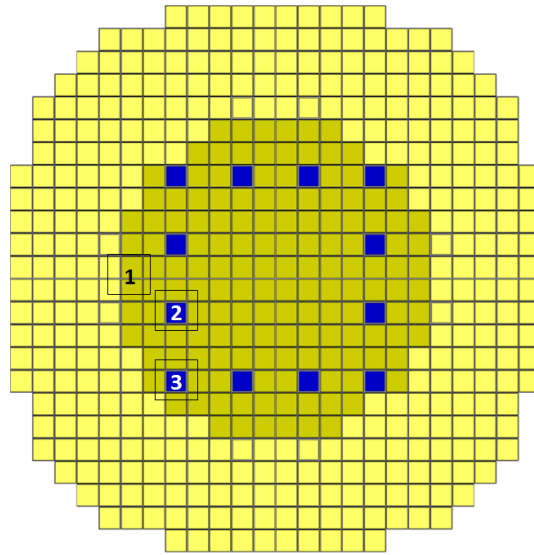


Figure 12: Hypothetical miniature fission chamber locations in SNEAK-12A core

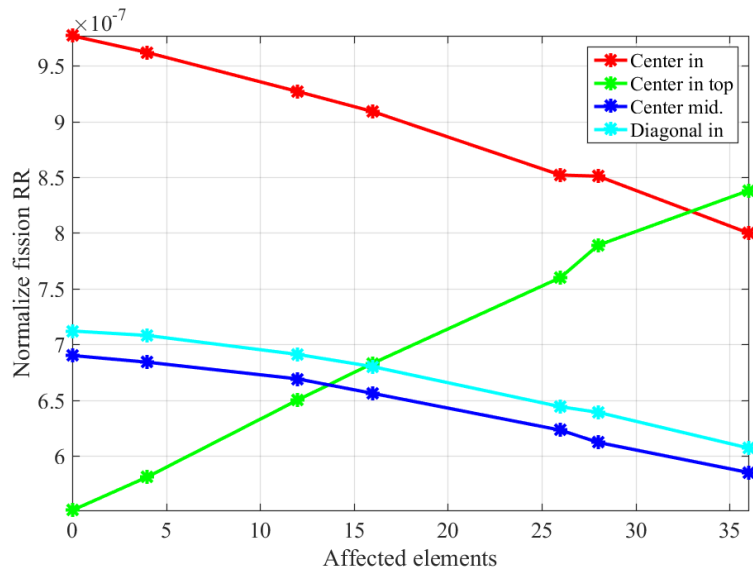


Figure 13: Fission reaction rates in ^{235}U detector as function of the number of affected fuel assemblies in molten pool configuration.

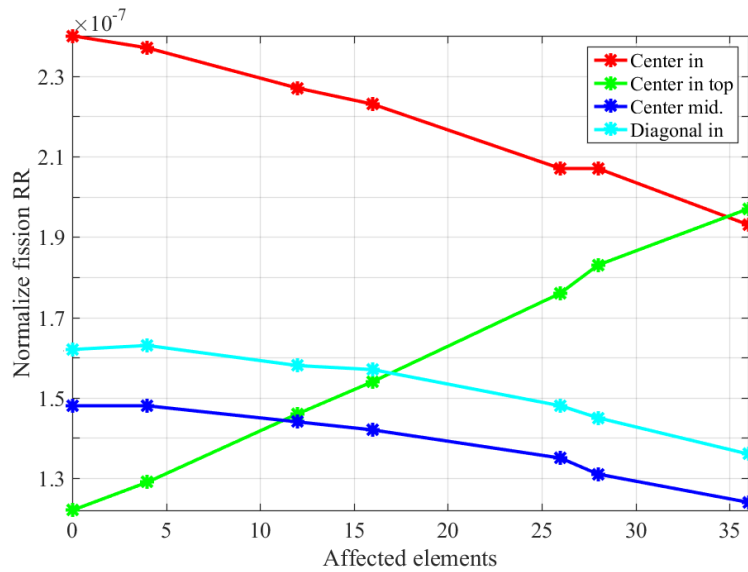


Figure 14: Fission reaction rates in ^{242}Pu detector as function of the number of affected fuel assemblies in molten pool configuration.

tions of reactivity changes as a results of disturbed core configurations, representing relocation of important materials (fuel, sodium, steel, aluminum) that could occur in the course of accident progression. The data obtained from the SNEDAX data base is presented in this paper in the form of a Monte Carlo codes benchmark problem.

The result of the benchmark showed that the reactivity effects of all unperturbed and distorted configurations could be well predicted by the MC codes - MCNP, Tripoli, and Serpent. The results obtained with the deterministic code ERANOS in R-Z geometry showed a good agreement for small configurations (4 and 12 affected elements), with a larger deviation for larger configuration (28 affected elements). From an extrapolation of those results (Fig. 7 it can be seen that ERANOS over estimates the positive reactivity changes region. This expected behavior is similar to the original SIMMER-II transport calculations performed in the 80's.

The presented results could be used for validation of codes dedicated for future fast reactor design. Moreover, the neutronic phenomena and reactivity effects studied in this this research are expected to occur also in molten pool formation in other fast reactors. In this case, the physical quantities will depend on the specific geometry and composition of the core design.

However, since SNEAK-12A was loaded with enriched uranium fuel whereas future GEN-IV reactors would operate with plutonium fuel loading, there is a need to validate the neutronic phenomena and reactivity effects, presented in this study, under suitable conditions. Such work is underway with the SNEAK-12B experimental program where the core was loaded with plutonium fuel.

In the last part of this study, we suggested a possible methodology for early detection of severe accident progression and molten pool formation. This subject is of utmost importance regarding the safety of fast reactors and requires further investigation and detailed study. The results presented in this study constitute a “proof of concept” for the

suggested early detection and monitoring methodology that should be applied for monitoring core behavior in the course of a [SCA](#).

245 As mentioned above, a new benchmark based on the SNEAK-12B is currently under investigation. However, the examination of the SNEAK-12A program has not been finished, and further analysis is currently underway, which includes sensitivity analysis of the core reactivity coefficients and associated nuclear data propagated uncertainties. The complete results will be presented in a companion paper. This is a necessary research for future experimental programs to be proposed at CEA Cadarache, in particular in awaited innovative ZPR designs such as the ZEPHYR
250 project lead by CEA.

Acknowledgment

The authors would like to extend their gratitude to Dr. Gerald RIMPAULT, CEA Cadarache, for providing additional information regarding the operated experiments in the SNEAK facility.

The research was partially funded by the Israeli ministry of National Infrastructures, Energy and Water Resources
255 public tender 3/15.

AppendixA. Benchmark full specification

This appendix brings the detailed specification of the different fuel assemblies loaded in to the [SNEAK-12A](#) core. The benchmark specifies three different levels of geometries. The first is the platelet, this is the most basic geometry and it consists of one plate. The second level is the cell, which is a combination of several platelets. The last level of the geometry is the assembly. An assembly is a combination of multiple cells stacked in a vertical greed. An example was shown in [Fig. 2](#). All the fuel cells have the same basic X-Y cross section, the platelet is $5.08 \times 5.08 \text{ cm}^2$, the cladding width is 0.28 cm with the remaining 0.08 cm occupied by air, making the total assembly X-Y cross section to be $5.44 \times 5.44 \text{ cm}^2$. For the smaller platelets loaded in the shim rods assemblies the cross section is $4.68 \times 4.68 \text{ cm}^2$ loaded in to a 0.68 cm thick can, when the outer region filled by air up to the total assembly X-Y cross section $5.44 \times 5.44 \text{ cm}^2$.

AppendixA.1. Assembly 12A-11-01 - Radial blanket assembly

The radial blanket consists purely of depleted uranium. The assembly axial cross section is shown in [Fig. A.15](#) with the dimensions given in [Table A.5](#) and material balance in [Table A.6](#).

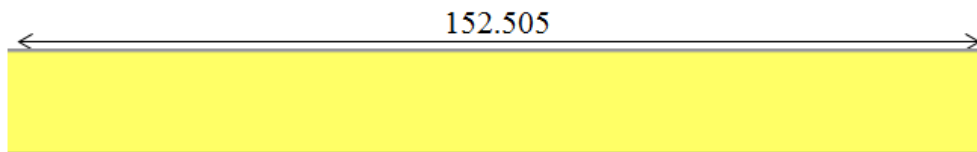


Figure A.15: Axial cross section of blanket fuel assembly.

Table A.5: Assembly 12A-11-01 cell boundaries and platelets quantities.

Cell	From, cm	To, cm	Num. of ele.	ele. height, cm
BL-UDEPL1	-76.2526	76.2526	5	30.501

Table A.6: Assembly 12A-11-01 material balance, #/cm b.

Isotop	BL-UDEPL1
Ni	4.727237E-04
²³⁵ U	1.862878E-04
²³⁸ U	4.580126E-02

Appendix A.2. Assembly 12A-10-01 - Normal core assembly

270 The normal core assembly is a complex assembly made to simulate interactions between the fuel and the sodium, shown in Fig. A.16. Therefore, plates of enriched fuel, to level of 35% and 20%, were separated by solid sodium plate (Natrium), as it can be seen in Fig. A.17a. The assembly is reflected by an axial reflector, which consists of sodium and natural UO₂, as can be seen in Fig. A.17b. The quantities and the axial dimensions of the cells and the composing platelets is summarized in Table A.7 and Table A.8, where Table A.9 contains the material compositions of all the
 275 different platelets.

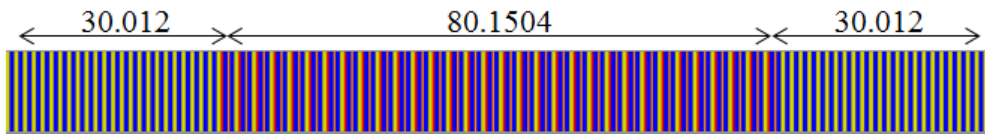


Figure A.16: Axial cross section of normal core assembly.

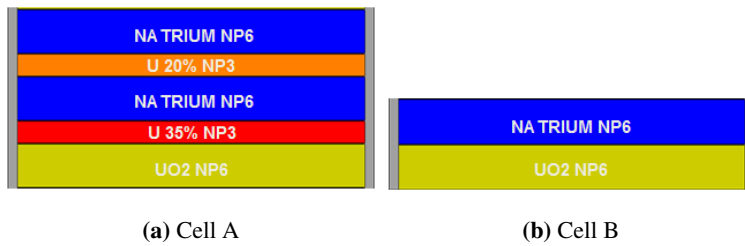


Figure A.17: Composing cells of assembly 12A-10-01.

Table A.7: Assembly 12A-10-01 cell boundaries and platelets quantities.

Cell	From, cm	To, cm	Num. of ele.	ele. height, cm
B	-70.08	-40.08	24	1.2505
A	-40.08	40.08	32	2.5047
B	40.08	70.08	24	1.2505

Table A.8: Assembly 12A-10-01 platelets boundaries.

Plate	From, cm	To, cm	ele. height, cm
Cell A			
UO2 NP6	0	0.6257	0.6257
U 35% NP3	0.6257	0.9401	0.3144
NATRIUM NP6	0.9401	1.5649	0.6248
U 20% NP6	1.5649	1.8799	0.3150
NATRIUM NP6	1.8799	2.5047	0.6248
Cell B			
UO2 NP6	0	0.6257	0.6257
NATRIUM NP6	0.6257	1.2505	0.6248

Table A.9: Assembly 12A-10-01 material balance, #/cm b.

Isotop	UO2 NP6	U35% NP3	NATRIUM NP6	U20% NP3
Al	1.380427E-05	-	-	-
C	6.399417E-05	-	4.371840E-04	-
Cr	1.944067E-03	-	3.584877E-02	-
Fe	6.886453E-03	-	1.259854E-01	-
H	1.765199E-05	-	-	-
Mg	6.123131E-06	-	-	-
Mn	4.007326E-05	-	6.832343E-04	-
Mo	1.126957E-05	-	2.621876E-04	-
Na	-	-	3.082528E-01	-
Nb	5.553869E-07	-	-	-
Ni	1.018455E-03	8.092385E-04	2.369649E-02	8.077022E-04
O	3.990924E-02	-	5.707915E-06	-
P	2.768817E-05	-	1.830844E-03	-
S	1.054332E-06	-	5.586765E-05	-
Si	8.818426E-05	-	2.159033E-02	-
²³⁵ U	1.432592E-04	1.689311E-02	-	9.292719E-03
²³⁸ U	1.975188E-02	3.001687E-02	-	3.706167E-02

Appendix A.3. Assembly 12A-10-90 - Edge element assembly

Assembly 12A-90-10 only modification in respect to assembly 12A-10-01 is in the axial blanket assembly, as it can be seen in Fig. A.18 and Fig. A.19. The difference in the material composition is not that substantial. However, in order to achieve higher accuracy of the calculations it was not neglected. Table A.10 and Table A.11 summarize the amounts of each platelets and cells in the fuel assembly and their boundaries, where Table A.12 contains the material balance.

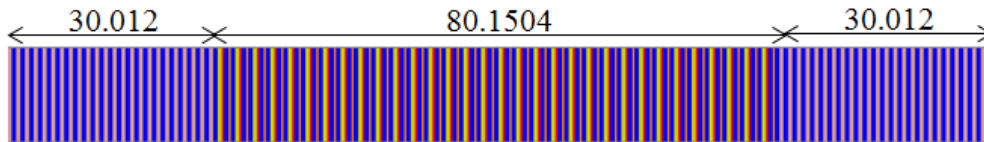


Figure A.18: Axial cross section of edge element assembly.

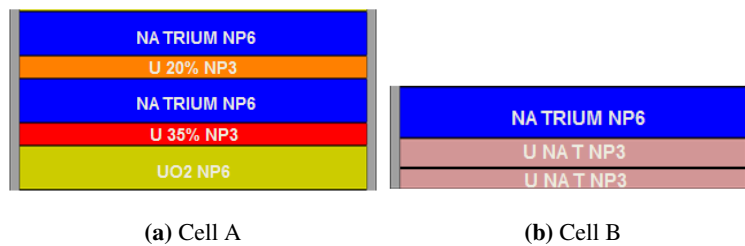


Figure A.19: Composing cells of assembly 12A-10-90.

Table A.10: Assembly 12A-10-90 cell boundaries and platelets quantities.

Cell	From, cm	To, cm	Num. of ele.	ele. height, cm
BM	-70.08	-40.08	24	1.2505
A	-40.08	40.08	32	2.5047
BM	40.08	70.08	24	1.2505

Table A.11: Assembly 12A-10-90 platelets boundaries.

Plate	From, cm	To, cm	ele. height, cm
Cell A			
UO2 NP6	0	0.6257	0.6257
U 35% NP3	0.6257	0.9401	0.3144
NATRIUM NP6	0.9401	1.5649	0.6248
U 20% NP6	1.5649	1.8799	0.3150
NATRIUM NP6	1.8799	2.5047	0.6248
Cell BM			
U NAT NP3	0	0.3134	0.3134
U NAT NP3	0.3134	0.6268	0.3134
NATRIUM NP6	0.6268	1.2505	0.6237

Table A.12: Assembly 12A-10-90 material balance, #/cm b.

Isotop	UO2 NP6	U35% NP3	NATRIUM NP6	U20% NP3	U NAT NP3
Al	1.380427E-05	-	-	-	-
C	6.399417E-05	-	4.371840E-04	-	-
Cr	1.944067E-03	-	3.584877E-02	-	-
Fe	6.886453E-03	-	1.259854E-01	-	-
H	1.765199E-05	-	-	-	-
Mg	6.123131E-06	-	-	-	-
Mn	4.007326E-05	-	6.832343E-04	-	-
Mo	1.126957E-05	-	2.621876E-04	-	-
Na	-	-	3.082528E-01	-	-
Nb	5.553869E-07	-	-	-	-
Ni	1.018455E-03	8.092385E-04	2.369649E-02	8.077022E-04	7.991457E-04
O	3.990924E-02	-	5.707915E-06	-	-
P	2.768817E-05	-	1.830844E-03	-	-
S	1.054332E-06	-	5.586765E-05	-	-
Si	8.818426E-05	-	2.159033E-02	-	-
²³⁵ U	1.432592E-04	1.689311E-02	-	9.292719E-03	3.352181E-04
²³⁸ U	1.975188E-02	3.001687E-02	-	3.706167E-02	4.619381E-02

Appendix A.4. Assembly 12A-12-01 - Core center region shim rod

The shim rods in the SNEAK core are made of a fissile material, therefore their insertion brings a positive reactivity feedback. As it was mentioned earlier, the X-Y cross section of the shim rods differs from the X-Y cross section of the fuel elements. Each shim rod has a $4.68 \times 4.68 \text{ cm}^2$ cross section. The geometry of the core shim rod shown in Fig A.20 and A.21, and dimensions summarized in Table A.18 and A.19. The material balance is summarized in Table A.15.

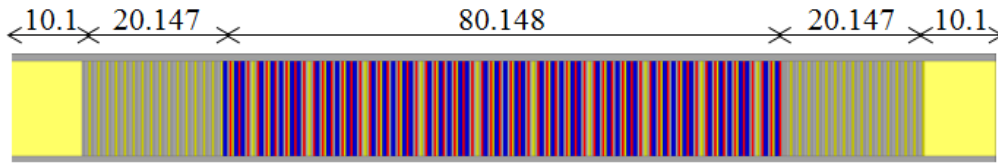


Figure A.20: Axial cross section of core shim rod assembly.

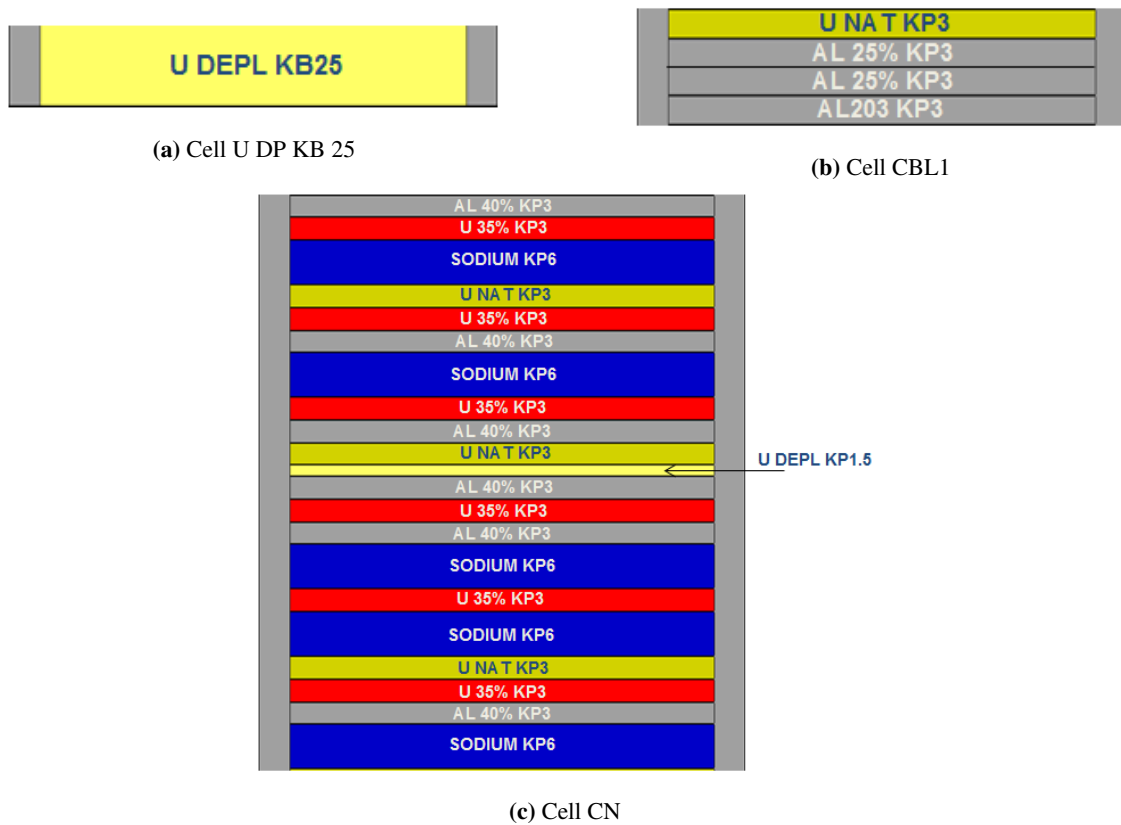


Figure A.21: Composing cells of assembly 12A-12-01.

Table A.13: Assembly 12A-12-01 cell boundaries and platelets quantities.

Cell	From, cm	To, cm	Num. of ele.	ele. height, cm
U DP KB25	-70.08	-60.08	4	2.532
CBL1	-60.08	-40.08	16	1.2592
CN	-40.08	40.08	10	8.0148
CBL1	40.08	60.08	16	1.2592
U DP KB25	60.08	70.08	4	2.532

Table A.14: Assembly 12A-12-01 platelets boundaries.

Plate	From, cm	To, cm	ele. height, cm
Cell U DP KB25			
U DEPL KB25	0	2.5320	2.5320
Cell CBL1			
AL203 KP3	0	0.3150	0.3150
AL 25% KP3	0.3150	0.6302	0.3152
AL 25% KP3	0.6302	0.9454	0.3152
U NAT KP3	0.9454	1.2592	0.3138
Cell CN			
SODIUM KP6	0	0.6280	0.6280
AL 40% KP3	0.6280	0.9440	0.3160
U 35% KP3	0.9440	1.2574	0.3134
U NAT KP3	1.2574	1.5712	0.3138
SODIUM KP6	1.5712	2.1992	0.6280
U 35% KP3	2.1992	2.5126	0.3134
SODIUM KP6	2.5126	3.1406	0.6280
AL 40% KP3	3.1406	3.4566	0.3160
U 35% KP3	3.4566	3.7700	0.3134
AL 40% KP3	3.7700	4.0860	0.3160
U DEPL KP1.5	4.0860	4.2430	0.1570
U NAT KP3	4.2430	4.5568	0.3138
AL 40% KP3	4.5568	4.8728	0.3160
U 35% KP3	4.8728	5.1862	0.3134
SODIUM KP6	5.1862	5.8142	0.6280
AL 40% KP3	5.8142	6.1302	0.3160
U 35% KP3	6.1302	6.4436	0.3134
U NAT KP3	6.4436	6.7574	0.3138
SODIUM KP6	6.7574	7.3854	0.6280
U 35% KP3	7.3854	7.6988	0.3134
AL 40% KP3	7.6988	8.0148	0.3160

Table A.15: Assembly 12A-12-01 material balance, #/cm b.

Isotop	AL203 KP3	AL 25% KP3	U NAT KP3	SODIUM KP6	AL 40% KP3
Al	4.473958E-02	9.730417E-02	-	-	2.296403E-02
C	-	-	-	3.281205E-05	-
Cr	-	-	-	2.274693E-03	-
Fe	-	-	-	7.948392E-03	-
H	-	-	-	-	-
Mg	1.702613E-04	9.964209E-04	-	-	2.351786E-04
Mn	-	3.528015E-04	-	4.224415E-05	8.325855E-05
Mo	-	-	-	1.734453E-05	-
Na	-	-	-	1.899775E-02	-
Nb	-	-	-	-	-
Ni	-	-	1.343404E-03	1.493208E-03	-
O	6.727969E-02	-	-	-	-
P	-	-	-	-	-
S	-	8.147019E-04	-	4.095983E-06	-
Si	-	-	-	1.481138E-04	1.922626E-04
U235	-	-	3.325779E-04	-	-
U238	-	-	4.580041E-02	-	-
Isotop	U 35% KP3	U DEPL KB25	U DEPL KP1.5		
Ni	9.565251E-04	2.404915E-04	1.819886E-03		
U235	1.689129E-02	1.906997E-04	1.818333E-04		
U238	2.988937E-02	4.688144E-02	4.474099E-02		

Appendix A.5. Assembly 12A-12-02 - Blanket region shim rod

The blanket region shim rod consist of a single material, just as the blanket assemblies, shown if Fig. A.22. All
 290 the parameters summarized in Tables A.16 and A.17.

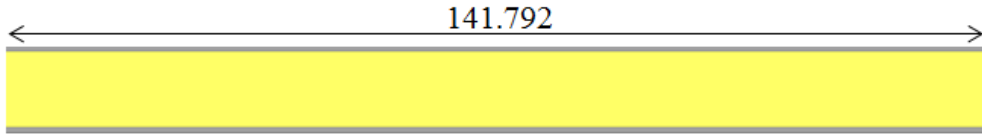


Figure A.22: Axial cross section of blanket shim rod assembly.

Table A.16: Assembly 12A-12-02 cell boundaries and platelets quantities.

Cell	From, cm	To, cm	Num. of ele.	ele. height, cm
U DP KB25	-70.08	71.712	56	2.532

Table A.17: Assembly 12A-12-02 material balance, #/cm b.

Isotop	U DEPL KB25
Ni	2.404915E-04
²³⁵ U	1.906997E-04
²³⁵ U	4.688144E-02

Appendix A.6. Assemblies 12A-13-01 and 12A-13-02 - Core's driver and safety rod

Those assemblies have almost the same distribution of material and geometry as the 12A-12-01 shim rod. The main difference is lower aluminum quantity and sodium presence in the axial blanket. The safety rods in the SNEAK-12A geometry are constantly in their most inner position inside the core. The geometry is show in Fig. A.23 and A.24, and summarized in Table A.20 and A.25. The material balance can be found in Table A.15, this is the same material balance a for the core center region shim rod.

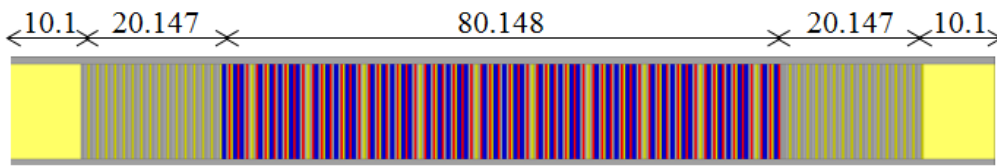


Figure A.23: Axial cross section of driver and safety shim rods assemblies.

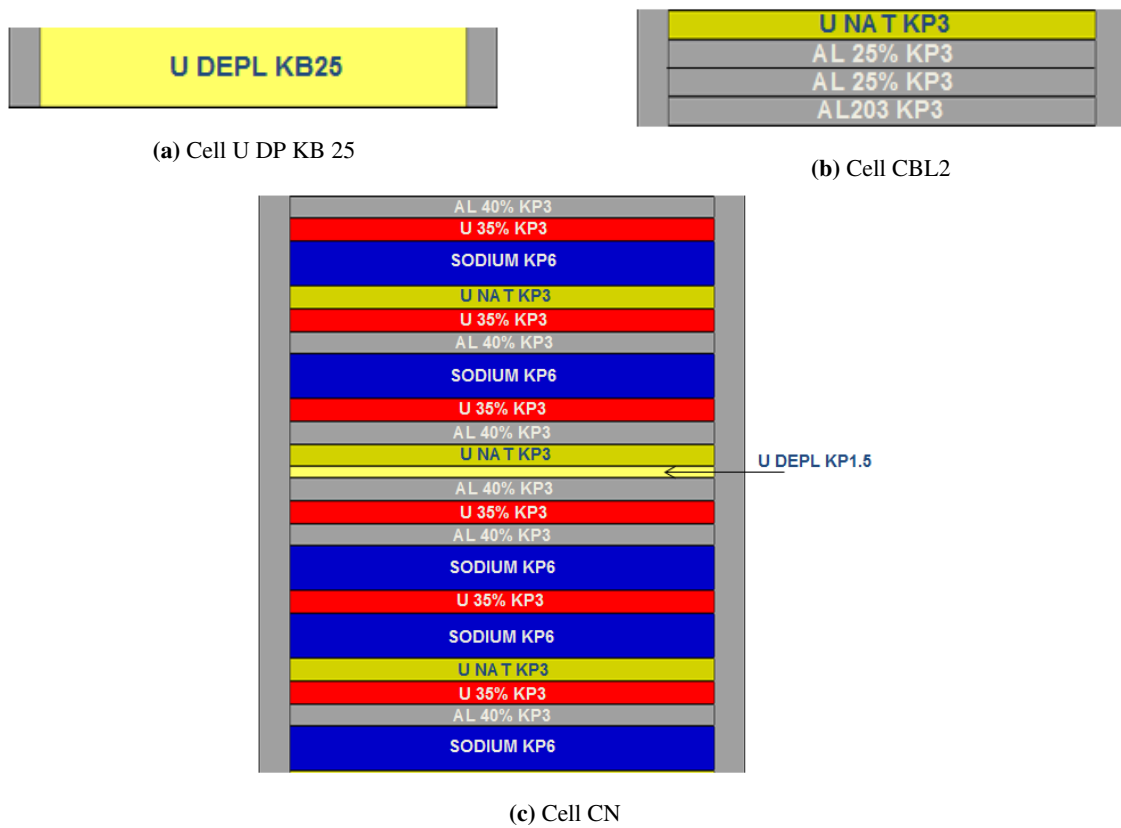


Figure A.24: Composing cells of assemblies 12A-13-01/2.

Table A.18: Assembly 12A-12-01 cell boundaries and platelets quantities.

Cell	From, cm	To, cm	Num. of ele.	ele. height, cm
U DP KB25	-70.08	-60.08	4	2.532
CBL2	-60.08	-40.08	16	1.257
CN	-40.08	40.08	10	8.0148
CBL2	40.08	60.08	16	1.257
U DP KB25	60.08	70.08	4	2.532

Table A.19: Assembly 12A-12-01 platelets boundaries.

Plate	From, cm	To, cm	ele. height, cm
Cell U DP KB25			
U DEPL KB25	0	2.5320	2.5320
Cell CBL1			
U NAT KP3	0	0.3138	0.3138
AL 25% KP3	0.3138	0.6290	0.3152
SODIUM KP6	0.6290	1.2570	0.6280
Cell CN			
SODIUM KP6	0	0.6280	0.6280
AL 40% KP3	0.6280	0.9440	0.3160
U 35% KP3	0.9440	1.2574	0.3134
U NAT KP3	1.2574	1.5712	0.3138
SODIUM KP6	1.5712	2.1992	0.6280
U 35% KP3	2.1992	2.5126	0.3134
SODIUM KP6	2.5126	3.1406	0.6280
AL 40% KP3	3.1406	3.4566	0.3160
U 35% KP3	3.4566	3.7700	0.3134
AL 40% KP3	3.7700	4.0860	0.3160
U DEPL KP1.5	4.0860	4.2430	0.1570
U NAT KP3	4.2430	4.5568	0.3138
AL 40% KP3	4.5568	4.8728	0.3160
U 35% KP3	4.8728	5.1862	0.3134
SODIUM KP6	5.1862	5.8142	0.6280
AL 40% KP3	5.8142	6.1302	0.3160
U 35% KP3	6.1302	6.4436	0.3134
U NAT KP3	6.4436	6.7574	0.3138
SODIUM KP6	6.7574	7.3854	0.6280
U 35% KP3	7.3854	7.6988	0.3134
AL 40% KP3	7.6988	8.0148	0.3160

Appendix A.7. Assembly 12A-10-26 - Small slump-in configuration

This fuel assembly is designated for simulation of small fuel slump-in in the center of the core. As it can be seen in Fig. A.25 and A.26, the fuel is being compacted in the center, while on both sides a voided region (simulated by empty steel cans) is formatted. The rest of the fuel assembly is similar to assembly 12A-10-01 with a single modification, replacement of the sodium plates by voided steel boxes. The dimensions are summarized in Tables A.20 and ?? with the material balance shown in Table A.22.

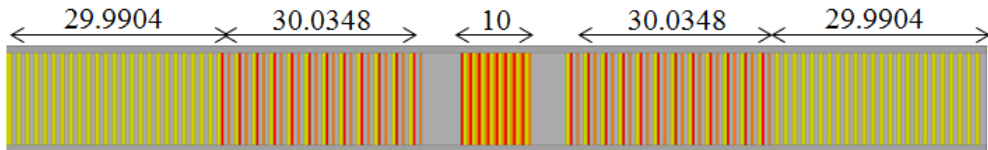


Figure A.25: Axial cross section of small slump in configuration.

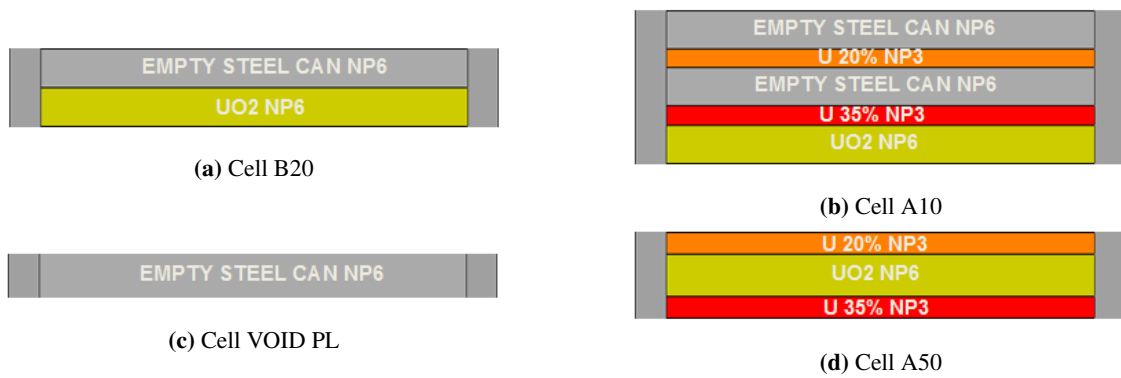


Figure A.26: Composing cells of assemblies 12A-10-26.

Table A.20: Assembly 12A-10-26 cell boundaries and platelets quantities.

Cell	From, cm	To, cm	Num. of ele.	ele. height, cm
B20	-70.0368	-40.0464	24	1.2496
A10	-40.0464	-10.0116	12	2.5029
VOID-PL	-10.0116	-5.0204	8	0.6239
A50	-5.0204	5.0204	8	1.2551
VOID-PL	5.0204	10.0116	8	0.6239
A10	10.0116	40.0464	12	2.5029
B20	40.0464	-70.0368	24	1.2496

Table A.21: Assembly 12A-10-26 platelets boundaries.

Plate	From, cm	To, cm	ele. height, cm
Cell VOID PL			
EMPTY STEEL CAN NP6	0	0.6239	0.6239
Cell B20			
UO2 NP6	0	0.6257	0.6257
EMPTY STEEL CAN NP6	0.6257	1.2496	0.6239
Cell A10			
UO2 NP6	0	0.6257	0.6257
U 35% NP3	0.6257	0.9401	0.3144
EMPTY STEEL CAN NP6	0.9401	1.5640	0.6239
U 20% NP3	1.5640	1.8790	0.3150
EMPTY STEEL CAN NP6	1.8790	2.5029	0.6239
Cell A50			
U 35% NP3	0	0.3144	0.3144
UO2 NP6	0.3144	0.9401	0.6239
U 20% NP3	0.9401	1.2551	0.3150

Table A.22: Assembly 12A-12-01 material balance, #/cm b.

Isotop	UO2 NP6	U35% NP3	EMPTY STEEL CAN NP6	U 20% NP3
Al	1.380427E-05	-	-	-
C	6.399417E-05	-	3.34349E-05	-
Cr	1.944067E-03	-	2.18587E-03	-
Fe	6.886453E-03	-	7.62764E-03	-
H	1.765199E-05	-	-	-
Mg	6.123131E-06	-	-	-
Mn	4.007326E-05	-	3.82865E-05	-
Mo	1.126957E-05	-	1.66099E-05	-
Na	-	-	-	-
Nb	5.553869E-07	-	-	-
Ni	1.018455E-03	8.092385E-04	1.45817E-03	8.077022E-04
O	3.990924E-02	-	-	-
P	2.768817E-05	-	1.21425E-04	-
S	1.054332E-06	-	4.17887E-06	-
Si	8.818426E-05	-	1.49793E-04	-
U235	1.432592E-04	1.689311E-02	-	9.292719E-03
U238	1.975188E-02	3.001687E-02	-	3.706167E-02

Appendix A.8. Assembly 12A-10-27 - Small slump-in configuration

The fuel assembly 12A-10-27 aim is to simulate large slump in, shown in Fig. A.27, where assembly configuration
 305 is summarized in Table A.23. The cell dimensions can be taken from Table A.25 and material distribution from Table
 A.22.

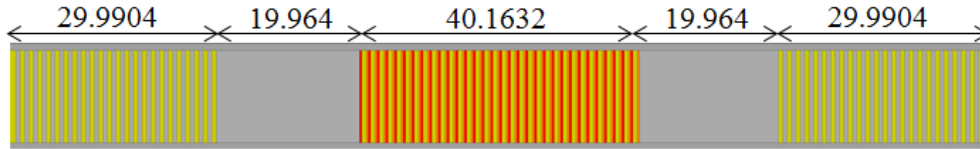


Figure A.27: Axial cross section of large slump in configuration.

Table A.23: Assembly 12A-10-27 cell boundaries and platelets quantities.

Cell	From, cm	To, cm	Num. of ele.	ele. height, cm
B20	-70.0368	-40.0464	24	1.2496
VOID-PL	-40.0464	-20.0816	32	0.6239
A50	-20.0816	20.0816	32	1.2551
VOID-PL	20.0816	40.0464	32	0.6239
B20	40.0464	70.0368	24	1.2496

Appendix A.9. Assembly 12A-10-96 - Small slump-in configuration

The last configuration in the SNEAK-12A that would be observed here is the one simulation molten pool. The material composition can be taken from Table A.22 and most of the composing cells (A50, B20 and Empty Steel Cans) can be found in the definition of assembly 12A-10-26 (small slump-in). The assembly 12A-10-96 can be seen in Fig. A.29. The molten pool configuration contains additional cell, that wasn't introduced previously, it is brought in Fig. A.29. The material balance for SUPPORT CAN NP6 is given in Table ??.



Figure A.28: Axial cross section of molten pool configuration.



Figure A.29: Cell B10.

Table A.24: Assembly 12A-10-96 cell boundaries and platelets quantities.

Cell	From, cm	To, cm	Num. of ele.	ele. height, cm
ST FLAME L	-73.5000	10.0100	1	83.510
A50	10.0100	40.1324	32	1.2551
B10	40.1324	60.1844	8	2.5065
B20	60.1844	70.1812	8	1.2496

Table A.25: Assembly 12A-10-26 platelets boundaries.

Plate	From, cm	To, cm	ele. height, cm
Cell ST FLAME L			
SUPPORT CAN NP6	0	83.51	83.51
Cell B20			
UO2 NP6	0	0.6257	0.6257
EMPTY STEEL CAN NP6	0.6257	1.2496	0.6239
Cell B10			
UO2 NP6	0	0.6257	0.6257
U 35% NP3	0.6257	0.9401	0.3144
UO2 NP6	0.9401	1.5657	0.6257
U 20% NP3	1.5657	1.8808	0.3150
UO2 NP6	1.8808	2.5065	0.6257
Cell A50			
U 35% NP3	0	0.3144	0.3144
UO2 NP6	0.3144	0.9401	0.6239
U 20% NP3	0.9401	1.2551	0.3150

Table A.26: Material balance of the empty steel support can, #/cm b.

Isotop	U SUPPORT CAN NP6
Fe	2.90200E-03
Si	4.65000E-05
Mn	3.54000E-05
Cr	8.08600E-04
Ni	3.59900E-04

AppendixA.10. Cladding

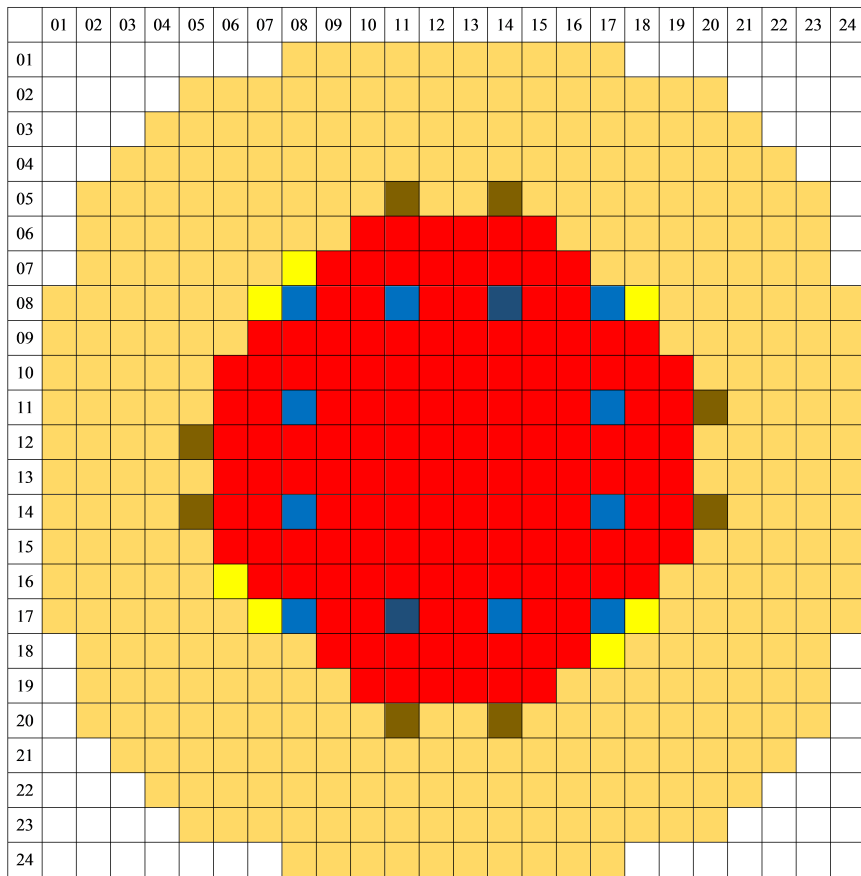
All the assemblies have the same cladding compositions, which is given in Table A.27.

Table A.27: Material balance for the assemblies steel cladding, #/cm b.

Isotop	CLADDING
C	4.0132580E-04
Fe	1.1703970E-01
Cr	3.2792630E-02
Mn	2.5873660E-03
Mo	2.9504490E-04
Nb	2.5284660E-04
Ni	1.6936410E-02
Si	1.3411650E-03

315 AppendixA.11. Basic core loading for the presented experiments

The basic loading pattern for the experiments presented in this paper is shown in Fig. ???. The core includes all the assemblies presented in the appendix. However, in order to determine the positions of the different experimental configuration involving material redistribution (e.g. molten pool, slump-in, etc.) it is required to review the Fig. 5 and 3.



Color	Assembly type
Yellow	Blanket assembly – 12A-11-01
Brown	Blanket shim rod – 12A-12-02
Red	Normal core assembly – 12A-10-01
Light Yellow	Edge element assemblies – 12A-10-90
Light Blue	Center core shim rod – 12A-12-01
Dark Blue	Driver/Safety shim rod – 12A-13-01/2

(b) Color map

(a) Core loading map

Figure A.30: Basic SNEAK-12A core loading for all the experimental configuration.

320 References

1. Ninokata H, Sawada T, Tomozoe H, Endo H, Shimizu A. A Study on Recriticality Characteristics of Fast Reactors in Pursuit of Recriticality-Accident-Free Concepts. *Progress in Nuclear Energy* 1995;29:387–93.
2. Helm F, Henneges G. Measurements and Calculation of Reactivity Effects of Material Rearrangements in a Plutonium-Fueled Fast Reactor Rod Lattice. *Nuclear Technology* 1985;71:68–81.
- 325 3. Henneges G. Validation of Neutronic Codes for Distorted Core Configurations with the SNEAK-12 Critical Assemblies. *Nuclear Science and Engineering* 1988;100:314–23.
4. Maschek W, Rineiski A, Suzuki T, Wang S, Mori M, Wiegner E, Wilhelm D, Kretschmar F. SIMMER-III and SIMMER-IV Safety Code Development for Reactors with Transmutation Capability. In: *Mathematics and Computation, Supercomputing, Reactor Physics and Biological Applications*. Avignon, France: American Nuclear Society; 2005:1–14.
- 330 5. Gunther E, Kinnebrock W. SNOW - ein zweidimensionales Sn0 Programm zur Lösung der Neutronentransportgleichung in Platten - und Zylindergeometrie. Tech. Rep.; 1977.
6. Kobayashi K. TP2-A computer program for the calculation of reactivity and kinetic parameters by the two dimensional transport perturbation theory. Tech. Rep.; 1973.
7. Riyas A, Mohanakrishnan P. ULOF transient behaviour of metal-fuelled fast breeder reactor cores as a function of core size and perturbation methods. *Nuclear Engineering and Design* 2014;278:141–9.
- 335 8. Suzuki T, Tobia Y, Kawada K, Tagami H, Sogabe J, Matsuba K, Ito K, Ohshima H. A preliminary evaluation of unprotected loss-of-flow accident for a prototype fast-breeder reactor. *Nuclear Engineering and Technology* 2015;47(3):240–52.
9. Sawada T, Ninokata H, Tomozoe H, Endo H. Recriticality characteristics of fast reactors and possibility of preclude recriticality by controlled material relocation. *Progress in Nuclear Energy* 1998;32(3/4):745–51.
- 340 10. Sawada T, Ninokata H, Tomozoe H. A recriticality-free fast reactor core concept. *Nuclear Technology* 2000;130(3):242–51.
11. Yamano H, Fujita S, Tobita Y, Sato I, Niwa H. Development of a three-dimensional CDA analysis code : SIMMER-IV and its first application to reactor case. *Nuclear Engineering and Design* 2008;238:66–73. doi:10.1016/j.nucengdes.2007.04.015.
12. Toibia Y, Yamano H, Sato I. Analytical study on elimination of severe recriticality in large small LMFBRs with enhancement of fuel discharge. *Nuclear Engineering and Design* 2007;238:57–65.
- 345 13. Konishi K, Toyooka Ji, Kamiyama K, Sato I, Kubo S, Kotake S, Koyama K, Vurim AD, Gaidaichuk VA, Pakhnits AV, Vassiliev YS. The result of a wall failure in-pile experiment under the EAGLE project. *Nuclear Engineering and Design* 2007;237:2165–74. doi:10.1016/j.nucengdes.2007.03.012.
14. Collins PJ, Ingram G. Simulated meltdown and vapor explosion experiments in ZEBRA 8G and Zebra 12 and their interpretation. In: *Proc. Int. Symp. Physics Fast Reactors*. Tokyo, Japan: American Nuclear Society; 1973:.
- 350 15. Kaiser RE, Beck CL, Lineberry MJ. Simulation of an HCDA sequence on the ZPPR critical facility. In: *Proc. ANS/ENG Mtg. Fast Reactors Safety and Related Physics*. Chicago, IL, USA: American Nuclear Society; 1976:.
16. Curtis R, Kelber C, Gelbard E, LeSage L, Luck L, Smith LR, Wade D. The use of benchmark criticals in fast reactor code validation. In: *Proc. Int. Symp. Fast Reactor Physics*. Aix en Provence, France: American Nuclear Society; 1979:.
17. Nakano M, Tsunoda H, Hirota J. An Experimental Study of Reactivity Changes and Flux Distortion in Simulated LMFBR Meltdown Cores. *Nuclear Science and Engineering* 1984;294:283–94.
- 355 18. Blaise P, Boussard F, Ros P, Leconte P, Margulis M, Martin G, Blandin K. Advanced small and large core distortion modeling in ZPR to assess core recriticality scenarios of SFR core degradation sequences. In: *Proc. Int. Conf. IGORR-2016*. Berlin Germany: European Nuclear Society; 2016:.
19. Helm F. The SNEDAX data base - General description and users instruction. Tech. Rep.; Forschungszeentrum Karlsruhe; Karlsruhe, Germany; 1996.
- 360 20. Helm F, Henneges G, Maschek W. Measurements and Computation of the Reactivity Effects of Accident-Caused Core Distortions in Liquid-Metal Fast Breeder Reactors. *Nuclear Science and Engineering* 1984;87:295–313.

21. Team XMC. MCNP - A General Monte Carlo N-Particle Transport Code, Version 5. Tech. Rep. April; 2003.
22. Brun E, Damian F, Diop CM, Dumonteil E, Hugot FX, Jouanne C, Lee YK, Malvagi F, Mazzolo A, Petit O, Trama JC, Visonneau T, Zoia A. TRIPOLI-4, CEA, EDF and AREVA reference Monte Carlo code. *Annals of Nuclear Energy* 2015;82:151–60.
23. Leppanen J, Pusa M, Viitanen T, Valtavirta V, Kaltiaisenaho T. The Serpent Monte Carlo code: Status, development and applications in 2013. *Annals of Nuclear Energy* 2015;82:142–50.
24. Ruggieri JM, Tommasi J and Lebart JF, Suteau C, Plisson-Rieunier D, De Saint Jean C, Rimpault G, Sublet JC. ERANOS 2.1: International Code System for GEN IV Fast reactor Analysis. In: *Proc. ICAAP2006*. Reno, NV, USA: American Nuclear Society; 1973:.
25. Tommasi J, Archier P, Rimpault G. Sodium void validation with ERANOS on zero power facility experiments. In: *Proc. PHYSOR-2010*. Pittsburg,PA,USA: American Nuclear Society; 2010:.
26. Kondo S, Turutani A, Ishikawa M. SIMMER-II application and validation studies in Japan for energetic accommodation of severe LFMFR accidents. In: *Proc. of the Int. Topic Meeting on Fast Reactor Safety*. Knoxville, TEN,USA: American Nuclear Society; 1985:.
27. Kayser G, Cadarache CE. The reactivity risk in fast reactors and the related international experimental programmes CABRI and SCARABEE. *Progress in Nuclear Energy* 2000;32(3/4):631–8.
28. Tobita Y, Yamano H, Sato I. Analytical study on elimination of severe recriticalities in large scale LMFBRs with enhancement of fuel discharge. *Nuclear Engineering and Design* 2008;238:57–65. doi:[10.1016/j.nucengdes.2007.04.014](https://doi.org/10.1016/j.nucengdes.2007.04.014).
29. Barre B. The future of CAPRA. Tech. Rep.; 1998.
30. Filliatre P, Oril L, Jammes C, Vermeeren L. Reasons why Plutonium-242 is the best fission chamber deposit to monitor the fast component of high neutron flux. *Nuclear Instruments and Methods in Physics Research A* 2008;593:510–8.